Numerical analysis of the influence of ball-joint clearance on the elastohydrodynamic performance of slipper interfaces in axial piston motors

Julien Ntede Florent[1,2], Ishan Suvarna[1], Lizhi Shang[1], Andrea De Pascale[2], Davide Moro[2], Alberto Gatti[3]

[1]*Maha Fluid Power Research Center, Purdue University, West Lafayette, Indiana 47906, USA,*
[2]*University of Bologna, Department of Industrial Engineering, 40136, Bologna, Italy,*
[3]*Hydraulic Motor Platform, Bonfiglioli Riduttori S.p.A. Via Enrico Mattei, 12 47122 Forlì (FC)*

Abstract

The tribological behavior of the slipper–swashplate interface is a primary factor limiting the operational lifespan and power density of swashplate axial piston motors. Under high hydraulic loading, the assumption of rigid body motion becomes invalid because elastic deformations within the slipper assembly substantially modify the geometry of the lubricating film. This study examines the typically overlooked influence of non-conformal contact mechanics in the piston-ball/slipper-socket joint and its role in driving deformation of the sealing land. Hertzian contact theory was employed to characterize the pressure distribution across the ball–socket interface, and a series of finite element simulations were conducted in ANSYS to quantify the effects of varying joint clearances. The results demonstrate that increasing the clearance significantly reduces the effective contact area, thereby generating localized stress concentrations. These stress concentrations impose a more concentrated mechanical load on the slipper body, inducing significant elastic warping and geometric nonlinearity across the sealing land interface.

The resulting increase in local contact pressures not only amplifies structural distortion but also may promote higher frictional losses within the ball–socket joint, as higher normal loads between relatively moving surfaces intensify boundary and mixed lubrication conditions. This effect contributes to greater energy dissipation and accelerated wear, further affecting the overall tribological performance of the assembly.

To evaluate the influence of structural deformation on the interface's load-carrying capacity, a hypothetical contact region was defined to simulate the mechanical interaction within the ball-socket joint. This was achieved by isolating the slipper and performing a parametric study in which the contact angle, measured radially from the central axis, was systematically varied. For each discrete angular increment, the specific pressure distribution required to equilibrate the piston's axial force was numerically determined and applied as the primary boundary condition. A comparative analysis shows that a clearance of 15 µm, corresponding to a contact angle of 60°, minimizes sealing land distortion. The resulting deformation field was then incorporated into the MULTICS Multiphysics framework to evaluate its influence on the load capacity of the slipper–swashplate interface.

Keywords: axial piston motor, ball socket interface, slipper swashplate interface, ball clearance

1. Introduction

Axial piston motors are central components in modern hydraulic systems due to their high-power density and dynamic performance. Their efficiency and durability depend strongly on the tribological behavior of internal interfaces, particularly the slipper–swashplate contact, where a micrometer-scale lubricating film must sustain high loads while limiting leakage and friction. As operating pressures and speeds continue to rise, accurately modeling the coupled fluid-structure interactions at this interface has become increasingly important. In most axial piston motor designs, the socket is located on the slipper side and is manufactured from a softer material such as brass, while the ball is integrated into the piston and made from a harder material such as steel. The ball diameter is typically a few micrometers smaller than the socket diameter. Experimental studies have shown that even a minor clearance offset has a significant influence on the performance and lubrication behavior of the slipper interface. For instance, abnormal changes or loosening at the ball-socket joint directly compromise the structural integrity and boundary conditions of the component, leading to premature fatigue or mechanical detachment under high-pressure dynamics [2]. However, despite its practical relevance, there is currently no systematic analysis or numerical model capable of fully explaining the physical mechanisms governing this effect. The objective of this work is therefore to investigate the influence of ball-socket geometry on slipper performance using a novel coupled simulation approach that captures the interaction between joint mechanics and the hydrodynamic behavior of the slipper–swashplate interface.

While early studies treated the slipper–swashplate gap as a classical hydrodynamic bearing, recent research has revealed a far more complex behavior. Wu et al. (2023) demonstrated that transient squeeze film effects induced by pressure pulsations can dominate the lubrication response, significantly altering film thickness and load capacity [1]. Geometric influences have also been emphasized: Haidak et al. (2018) showed that the ratio between the slipper's inner and outer diameters strongly affects power losses, identifying an optimal geometry that balances leakage control and viscous dissipation [3].

Slipper attitude and microgeometry further influence lubrication performance. Meng et al. (2020) found that small angular deviations can drastically modify pressure distribution and proposed a grooved sealing land design to enhance stability [4]. At the rough-surface scale, Sharif et al. (2012) analyzed mixed and micro EHL regimes, showing that decreasing the lambda ratio leads to asperity interactions and fatigue mechanisms not captured by smooth-surface models [5].

The piston–slipper joint introduces additional mechanical constraints. Shen et al. (2020) used dynamic simulation and ball-in-socket contact modeling to show that piston radius and radial clearance strongly influence contact stiffness, thereby affecting slipper motion and film formation [6]. Material innovation has also emerged as a promising direction: Schlegel and Schmitz (2025) demonstrated that high-performance plastics can replace copper-based slippers while maintaining acceptable deformation characteristics and reducing environmental impact [7]. Finally, Betti et al. (2026) extended Hertzian theory to conformal spherical contacts, providing improved stiffness predictions for geometries typical of piston–slipper joints [8].

Together, previous studies show that slipper–swashplate lubrication is governed by tightly coupled hydrodynamic, structural, and material effects. However, despite substantial progress, current models still struggle to capture the mechanical consequences of wear within the piston–slipper joint, particularly how increasing internal clearance modifies the deformation of the slipper sealing land and, in turn, the hydrodynamic performance of the interface. Most existing approaches treat the joint as perfectly rigid or impose simplified kinematic constraints that do not reflect the evolving geometry of worn components, leaving the relationship between internal joint clearance and external film behavior insufficiently quantified.

The present work addresses this gap by establishing, for the first time, a direct numerical link between ball–socket clearance and the resulting deformation of the sealing land. By parametrically reducing the contact angle, used here as an effective surrogate for increased joint clearance, the study reveals a clear transition in the deformation pattern from a stable, nearly uniform displacement field to a distinctly dished configuration. This shift has direct implications for film thickness distribution, load carrying capacity, and ultimately motor efficiency.

2. Mathematical model

The behavior of the slipper–swashplate interface fundamentally governs the tribological performance of an axial piston motor. Accurately predicting efficiency and durability requires a mathematical model that couples the slipper's motion and orientation with the fluid dynamics of the lubricating film. During operation, the slipper is subjected to time varying forces that continuously modify its attitude, making the local film thickness a dynamic quantity that must be evaluated at every point on the sealing land. This film thickness distribution is directly governed by the balance of forces acting on the piston–slipper assembly.

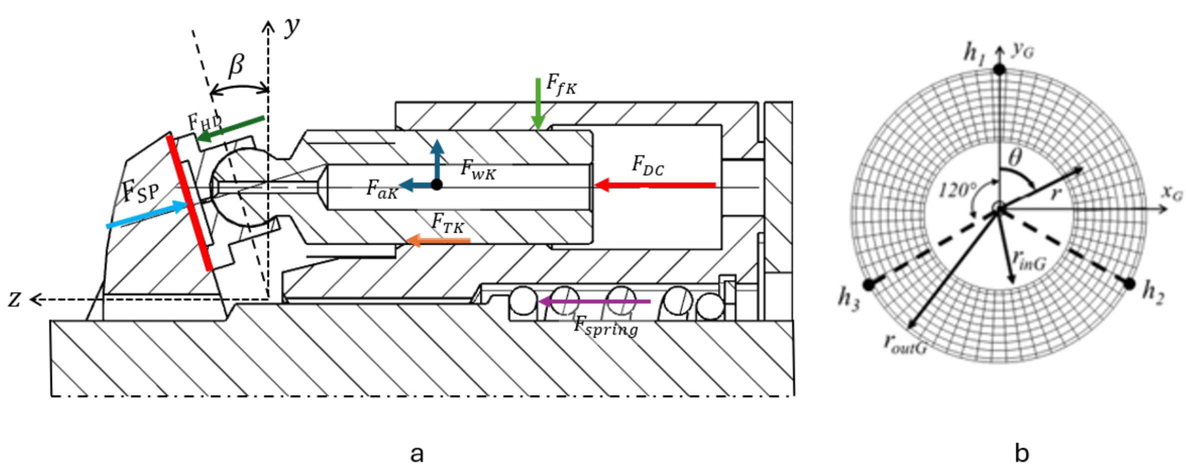

Figure 1: a) Dynamic force equilibrium of the piston-slipper assembly shown in an axial cross section of the motor, with the slipper–swashplate interface highlighted in red, the ball-joint inner lubrication channel, and the plate angle β indicated; b) slipper's sealing land frontal view with key variables for the oil film thickness in a local polar coordinate system

In the context of the slipper–swashplate interface, only the force components acting along the shaft axis (z coordinate in Figure 1a) contribute to the axial load on the slipper that determines the reaction pressure within the lubricating film. For this reason, the equilibrium is formulated exclusively along the shaft axis, where the dominant contributions arise from the hydraulic force generated by the chamber pressure F_{DC}, the inertial force F_{aK} associated with the reciprocating motion of the piston–slipper assembly, and the friction force F_{TK} transmitted through the piston and its bore. These three components constitute the primary load that must be supported by the hydrodynamic film at the slipper interface and therefore govern the resulting pressure distribution and tribological behavior. Based on the vectors defined in Figure 1a, the dynamic behavior of the piston-slipper assembly is governed by a single force balance equation along the piston axis. By accounting for both the external operating loads, fluid film reaction and the inertial effects, the complete dynamic equilibrium equation can be expressed as:

$$F_{DC} + F_{TK} + F_{HD} - F_{SP} \cdot cos\beta + F_{aK} = 0 \tag{1}$$

Where $F_{HD} = F_{spring}/z$.

In modelling the squeeze film effect, only the oil pressure acting on the piston and the swashplate reaction are considered, as the remaining forces affect only the magnitude of the compression force and do not influence the squeeze film mechanism itself.

The reaction force F_{SP} exerted by the swashplate on the slipper is the sum of two distinct contributions: the steady state hydrostatic support and the squeezed film effect, which are detailed in the following.

- The hydrostatic support force is governed by the pressure differential across the slipper's sealing land, which acts as the primary load bearing mechanism under steady state conditions. The fluid from the displacement chamber flows radially through the slipper's sealing land toward the low pressure region, generating a pressure gradient across the interface. The resulting pressure distribution over the sealing land, when integrated, yields the total hydrostatic lift force that stabilizes the slipper assembly:

$$F_{hyd} = \frac{\pi}{2}\left(\frac{r_{outG}^2 - r_{inG}^2}{ln(r_{outG}/r_{inG})}\right)p_{DC} \tag{2}$$

where r_{outG} and r_{inG} are external and internal radii of the sealing land, respectively, see Figure 1b, and p_{DC} is the chamber pressure.

- The squeeze film support force acts as a dynamic stabilizing mechanism that responds to the rapid, cyclic fluctuations inherent in hydraulic motor operation. As the piston reciprocates, the pressure in the chamber varies continuously, causing the slipper to move toward or away from the swashplate with a velocity $v = \frac{dh}{dt}$. Due to the lubricant's viscosity and near incompressibility, this motion generates a squeeze effect, producing a localized high-pressure film that provides additional hydrodynamic lift during pressure peaks expressed in polar coordinates as:

$$F_{squeeze} = \int_{r_{inG}}^{r_{outG}} \int_0^{2\pi} prdrd\theta \tag{3}$$

The fluid transport through the annular sealing land is modeled by considering a micro-elementary ring at a radius r with a radial width dr . Assuming steady, laminar, and isothermal flow, the volume flow rate q through this ring is governed by the pressure gradient term $\frac{dp}{dr}$.

The flow rate through the micro element ring at radius r is expressed as:

$$dq = -\frac{h^3}{12\mu}\left(2\pi r\frac{dp}{dr}\right)dr \tag{4}$$

Following the analytical formulation presented in [1], the pressure distribution along the radial land can be expressed analytically as:

$$p = \frac{3\mu}{h^3}\frac{dh}{dt}\left[\left(r^2 - r_{inG}^2\right) - \left(r_{outG}^2 - r_{inG}^2\right)\frac{ln(r/r_{inG})}{ln(r_{outG}/r_{inG})}\right] \tag{5}$$

Equation 3 can be rewritten as:

$$F_{squeeze} = \frac{3\pi\mu}{2h^3}\frac{dh}{dt}\left[r_{outG}^4 - r_{inG}^4 - \frac{\left(r_{outG}^2 - r_{inG}^2\right)^2}{ln(r_{outG}/r_{inG})}\right]cos\beta \tag{6}$$

The lubrication gap h deviates from a perfectly parallel configuration due to a complex nonlinear interaction between mechanical tilting moments, structural elasticity, and localized thermal expansion [3]. Consequently, in swashplate motors, the slipper orientation is inherently dynamic; continuously evolving in response to the transient pressure field and kinematic constraints.
The relationship between the slipper's tilt angle and interface performance is governed by a fundamental trade-off:

- Hydrodynamic enhancement: within a certain range, an increase in tilt angle promotes the formation of a converging-diverging wedge, enhancing the hydrodynamic lift and increasing the load carrying capacity of the oil film.
- Instability and leakage: conversely, excessive tilt leads to a pronounced film thickness gradient and an uneven pressure distribution. This condition increases the risk of local film rupture and significantly amplifies peripheral leakage, thereby reducing the motor's volumetric efficiency.

Furthermore, the mean film thickness introduces an additional optimization challenge. While a reduction in gap height enhances the squeeze film effect, providing damping and load carrying capacity, it also increases the viscous shear stress within the lubricant. This results in higher frictional losses and increased mechanical power dissipation. Most critically, excessively low film thickness shifts the lubrication regime toward boundary conditions, significantly increasing the likelihood of asperity contact and surface degradation.

To ensure the structural reliability of the axial piston motor, a stable lubrication regime must be maintained to prevent asperity contact between the slipper and the swashplate. This is achieved by ensuring that:

- The combined hydrodynamic and hydrostatic lift forces must exceed the net axial load acting on the slipper:

$$F_{squeeze} + F_{hyd} > F_{DC} + F_{ak} + F_{TK} + F_{HD} \tag{7}$$

- The minimum film thickness must satisfy the following condition:

$$h_{min} > \Lambda \cdot \left(\sigma_{slipper}^2 + \sigma_{sp}^2\right)^{1/2} \tag{8}$$

where Λ, referred to as the lambda ratio, and varies over the range $0.1 - 2.0$, is a parameter used to characterize the transition from full film lubrication to mixed and micro elastohydrodynamic lubrication regimes, and their associated fatigue damage [4].

The ball-socket clearance is a key design parameter governing the interfacial equilibrium of the slipper assembly. In addition to defining the kinematic range of the slipper tilt, it significantly affects the internal pressure distribution within the joint. Under high operating pressures, an improper clearance leads to localized elastic deformation, resulting in a crowning of the slipper sealing lands. Both insufficient and excessive clearance cause geometric distortion of the sealing land, disrupting the hydrostatic pressure balance and inducing fluid film instability. Therefore, the joint clearance becomes a critical factor in the transition from stable hydrodynamic lubrication to contact dominated regimes, characterized by asperity interaction and increased friction.

3. Numerical model of the ball-joint contact and simulation boundary conditions

To quantify the mechanical interactions governing load transfer from the piston ball to the slipper socket, the joint is modeled as a conformal spherical contact based on an extension of Hertzian contact theory. This approach is used to evaluate the resulting contact pressure distribution and the associated elastic distortion of the slipper, which directly affects the gap geometry [7]. The model is based on the following assumptions and boundary conditions:

- Linear elasticity and constitutive behavior: the piston ball and the slipper socket are modeled as homogeneous and isotropic continua. The material response follows Hooke's law, assuming that the stresses remain within the elastic regime and no plastic deformation occurs.
- Small displacement assumption: the contact radius is assumed to satisfy the condition $\delta \ll a \ll R_1$ (see Figure 2 for the meaning of the geometrical quantities). By ensuring that deformation remains localized, this justifies the use of small strain theory, whereby the global geometry of the components is not significantly altered.
- Frictionless contact interface: the contact between the ball and the socket is assumed to be frictionless ($\mu = 0$), allowing the analysis to focus solely on normal contact stresses and their role in transferring axial piston loads into structural deformation of the slipper sealing lands.

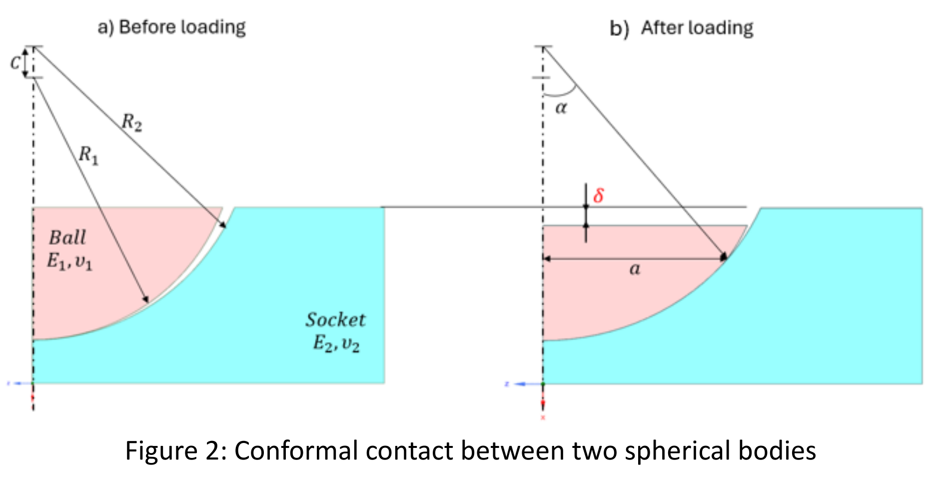

Figure 2: Conformal contact between two spherical bodies

While the frictionless assumption simplifies the formulation to isolate normal contact stresses, it introduces a limitation. In physical applications, hydrodynamic shear and boundary friction within the ball-socket joint generate tangential tractions. These tractions exert a micro tilting moment on the slipper body, which can slightly alter the symmetric bending of the sealing land.

Figure 2 illustrates the contact interface between the piston ball and the slipper socket, characterized by their respective radii of curvature, R_1 *and* R_2. According to Hertzian contact theory, the normal force F_n applied at the ball-and-socket interface results in a characteristic load displacement relationship. The corresponding compressive deformation δ, occurring along the loading direction, is given by [5]:

$$\delta = \left(\frac{9F_n^2}{16R'E'}\right)^{1/3} \tag{9}$$

Where $E' = 2\left(\frac{1-\upsilon_1^2}{E_1} + \frac{1-\upsilon_2^2}{E_2}\right)^{-1}$ is the equivalent elastic modulus, $R' = \frac{R_1 R_2}{R_2 - R_1} = \frac{(R_1 + C)R_1}{C}$ is the equivalent radius and C is the ball-joint clearance.

Based on contact equilibrium, the radius of the contact area a depends on the applied load and the geometric compatibility of the contacting surfaces, as given by:

$$a(\delta) = \sqrt{R'\delta} \tag{10}$$

The contact pressure distribution is not uniform and follows a semi-ellipsoidal profile. The maximum pressure, occurring at the center of the contact area, is a critical parameter for assessing the onset of local yielding. It is given by:

$$p_{max} = \left(\frac{6F_n E'}{\pi^2 (R')^2}\right)^{1/3} \tag{11}$$

p_{max} depends on the applied normal force as well as on the material and geometric properties. If it exceeds the yield strength of the socket material, localized plastic deformation may occur, permanently altering the socket geometry. As the ball is pressed into the socket, the resulting pressure is transmitted through the slipper thickness, leading to a slight deflection of the outer sealing lands.

To investigate the sensitivity of the slipper's structural integrity to joint tolerances, a high-fidelity finite element model was developed in ANSYS Mechanical. The model includes only the piston ball, socket, and slipper, as the deformation of the sealing land is governed by local contact mechanics rather than the global motor structure. The surrounding components, namely the cylinder block, the swashplate, and the housing, are orders of magnitude stiffer and therefore behave as rigid supports relative to the slipper. Modeling the entire motor would add computational cost without changing the deformation field of interest. For this reason, the cylinder side surface is fixed, while the slipper is allowed to translate in the plane but is constrained in the piston direction and in rotation, reproducing the effective kinematic environment imposed by the hydrodynamic film during operation. The simulation aims to characterize the mechanical coupling between the piston-ball interface and the resulting deformation of the slipper sealing land. A parametric study was conducted by keeping the socket geometry constant while varying the piston ball diameter, in order to obtain different ball-joint clearance values. To ensure accuracy and mesh independence of the structural quantities of interest, a mesh convergence study was performed. The final model utilizes high-order tetrahedral elements with an average global element size of 1.2 mm. Due to the high stress gradients and local contact conditions, local refinement was implemented at the ball-socket contact zone, where the element size was reduced to 0.1 mm. The mesh sensitivity evaluation demonstrated that further refining the contact zone element size to 0.08 mm resulted in less than a 1.2% variance in peak contact pressure and less than a 0.5% change in the maximum sealing land displacement, confirming that the main structural results are robustly mesh independent.

The piston–slipper relative motion was assumed to be no relative rotation for the structural finite element model. While physical slipper assemblies experience micro rotation relative to the piston during a complete shaft cycle, the macroscopic elastohydrodynamic loading acting on the slipper sealing land is axisymmetrically dominated during the high-pressure phase. Consequently, the localized stress concentrations and resulting dishing deformation profiles are rigidly linked to the slipper body itself and rotate concurrently with it relative to the swashplate interface. By locking the relative angular orientation between the piston ball and slipper socket during the static snapshot simulations, the model accurately isolates the structural compliance mode without sacrificing the fidelity of the transferred boundary conditions to the MULTICS framework.

The numerical model relies on standard industrial material configurations to accurately replicate load transfer and structural deflection. Table 1 lists the specific isotropic elastic properties applied to the components in the finite element framework. Among these parameters, the elastic modulus (E) of the bronze socket is the most critical for the subsequent analysis, as its lower stiffness directly governs the structural compliance, warping, and dishing characteristics of the slipper sealing land under high hydraulic forces.

Table 1: Material properties

$\boldsymbol{Material}$	$\boldsymbol{E(GPa)}$	$\boldsymbol{v}$
Structural steel	200	0.3
Bronze CuSn3Zn1	120	0.345

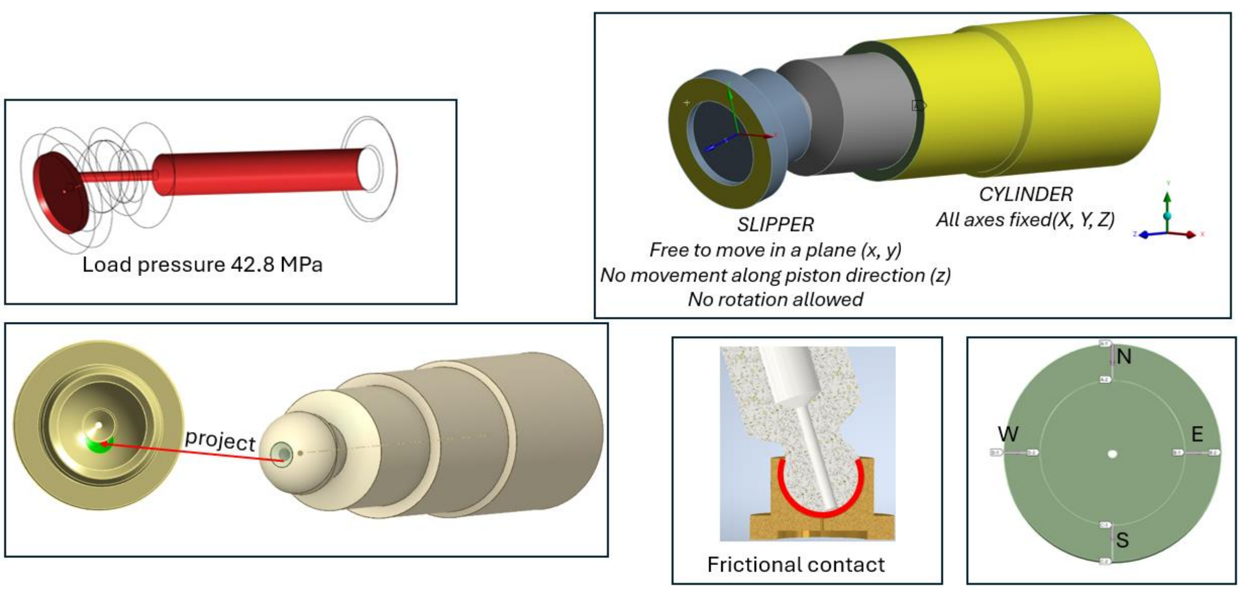

Figure 3: Simulation framework for structural compliance analysis, illustrating loading conditions and the location of node paths used for result extraction.

4. Results and discussion

i) Parametric FEM analysis of the joint clearance effect

The simulation results show a clear correlation between the joint clearance C and the interfacial contact pressure. This behavior is driven by the reduction in the effective contact area as the piston ball diameter decreases.

The contour plots in Figure 4 illustrate the local pressure distribution in the ball-socket joint and the peak pressure for four clearance levels, namely $0\ \mu m, 15\ \mu m, 35\ \mu m\ and\ 100\ \mu m$:

- $C = 0\ \mu m$: The contact pressure is distributed over a wider and more uniform area, resulting in relatively low peak pressure.
- $C = 100\ \mu m$: The contact area becomes highly localized near the apex of the socket. This concentration leads to a significant increase in peak pressure, reaching values as high as $804.79\ MPa$.

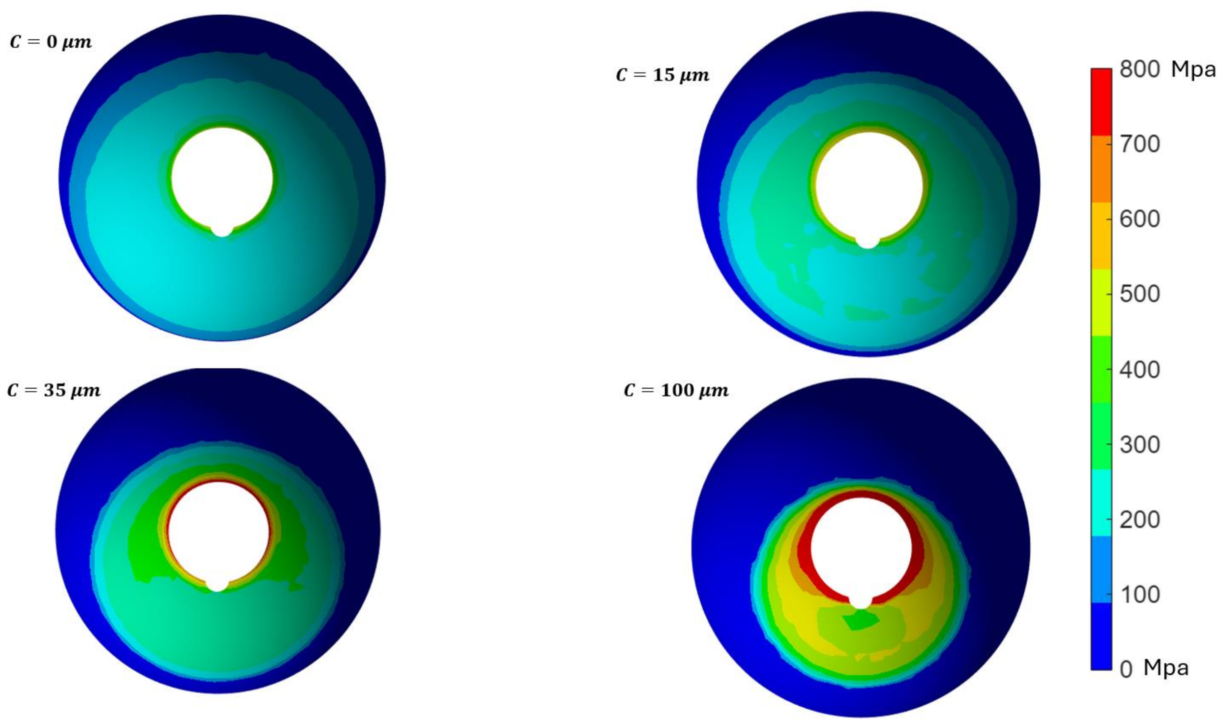

Figure 4. Comparative analysis of contact pressure distribution in the ball-socket interface: evolution of stress concentration and contact area reduction as a function of clearance

As clearance increases, the conformity between the ball and the socket diminishes, reducing the load bearing contact area. Since the axial hydraulic force F_{DC} remains constant across all cases, this reduction in contact area results in higher stress concentrations required to maintain equilibrium. Consequently, the peak contact pressure p_{max} increases accordingly. The increase in p_{max}, which approaches nearly three times its initial value, indicates a substantially higher local load on the bronze slipper and suggests that the material may approach its elastic limits in the most stressed regions. The associated pressure concentration also leads to non-uniform deformation of the slipper body, which in turn affects the stability of the lubrication film at the swashplate interface. The resulting deformation pattern along the sealing land exhibits a characteristic tilted shape (see Figure 5): the inner radius is displaced slightly downward due to the concentrated load transmitted through the ball–socket interface, while the outer radius shows a modest upward deflection caused by bending of the thin sealing land. This combination of central compression and peripheral lift-off represents the dominant deformation mode observed in the analysis.

This structural distortion also affects the hydraulic and tribological behavior of the interface. The slight lift of the outer radius increases the local gap height, promoting additional leakage through the sealing land. Conversely, the reduced film thickness near the inner radius brings the interface closer to mixed or boundary lubrication conditions, where the likelihood of localized wear and frictional heating becomes more significant. Together, these effects illustrate how even modest elastic deformation can subtly modify the operating conditions of the slipper–swashplate interface.

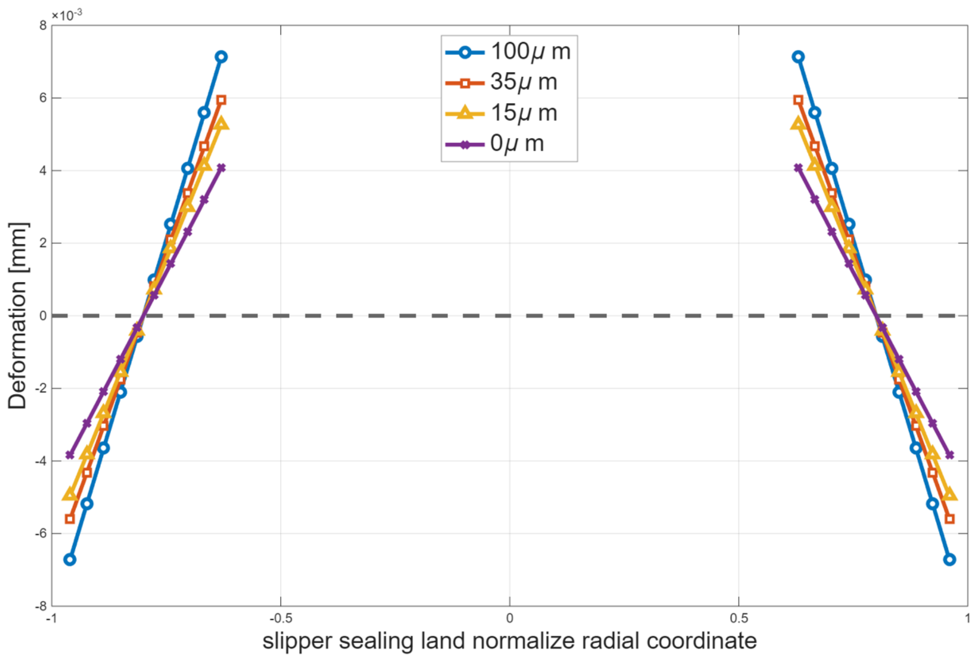

Figure 5. Structural deformation of the slipper sealing land

ii) Elastohydrodynamic and Structural Coupling in Piston-Slipper Interface Simulations

To quantify these coupled effects, the structural deformation is integrated into a fluid dynamic simulation using MULTICS, version 4.1.0 [15]. This is a multiphysics simulation environment for hydraulic machines developed at the Maha Fluid Research Center at Purdue University. Hydraulic units such as pumps and motors involve multiple interacting physical domains fluid chambers, lubricating films, and solid bodies as well as phenomena such as elastic deformation, fluid friction, and pressure induced motion. Multics incorporates dedicated physics models for each of these behaviors, and its modular architecture enables the addition and coupling of new models as needed. The tool, which has been successfully applied to a wide range of hydraulic units, including gear machines, gerotors, vane pumps, and axial piston machines [16], is used here to investigate the coupled fluid-structure problem at the slipper-swashplate interface, under dynamic conditions (Figure 6). In this study, the slipper–swashplate interface is modeled using the Reynolds equation, extended to account for asperity contact between the surfaces. The fluid dynamics within the pump/motor chambers and orifices are represented using a lumped parameter model, which significantly reduces computational cost compared to full CFD. The dynamics of the rotating components are also included and coupled with the fluid models, ensuring that all relevant interactions influencing the slipper–swashplate interface are captured. A dedicated timeline interpolation scheme ensures continuous data exchange between the models without increasing the overall simulation time.

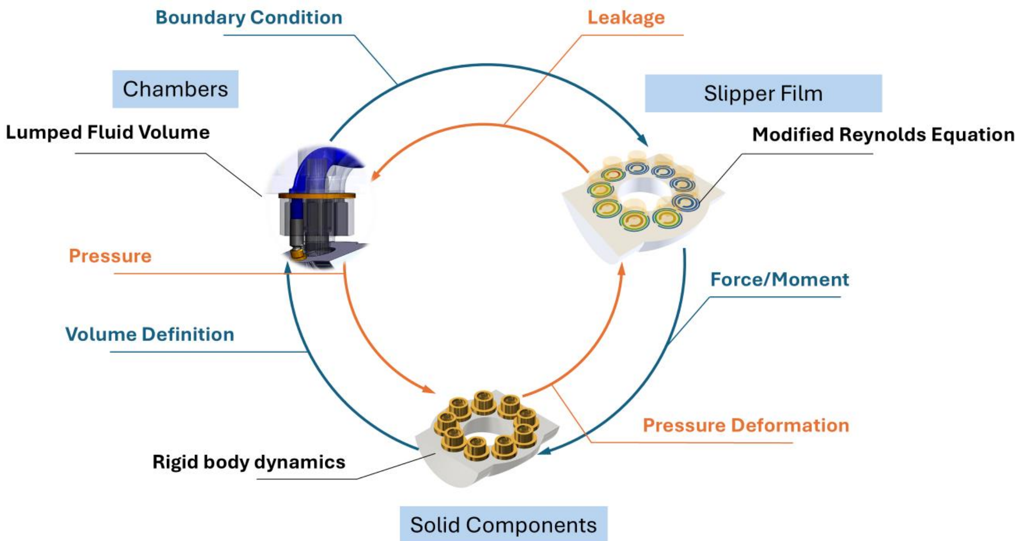

Figure 6. Multics Workflow for Coupled Fluid–Structure–Dynamics Simulation of the Slipper–Swashplate Lubrication Interface

Within Multics, the influence matrix method [17] is used to represent the elastic response of the slipper. This approach requires defining a representative contact area over which the piston ball pushes against the socket. While the effective contact area A_{eff} is directly obtained from the FEM simulations, the corresponding projected contact radius a (see Figure 2) needed for comparison with Hertzian analytical formulations is not explicitly provided [7]. To establish this connection, the contact between the piston ball (radius R_1) and the socket is approximated as occurring over a finite circular region characterized by a contact radius a, associated with a contact angle α. Assuming a constant piston force, the load is distributed over this effective area, allowing the corresponding contact pressure to be evaluated consistently in both the FEM based and Hertzian frameworks.

$$p_{contact} = \frac{F_{DC}/cos\beta}{A_{eff}} \tag{12}$$

The following geometric relations define the relationship between the simulated contact area and the projected contact radius:

$$A_{eff} = 2\pi R_2^2(1 - cos\alpha) \tag{13}$$

$$a = R_2 sin\alpha \tag{14}$$

Where α represents the contact half angle, defined as the angle between the axis of symmetry of the joint and the line connecting the center of the undeformed spherical socket to the boundary of the contact region (see Figure 2).

The proposed methodology maps physical joint clearance to an equivalent contact angle, establishing an effective geometric surrogate within the MULTICS framework. Although this approach leverages a statically equivalent, uniform pressure distribution over a predefined circular boundary, a primary limitation is its inability to dynamically capture the non-uniformity and inherent asymmetry of the contact patch. This limitation is particularly critical during high-speed tilting or transient dynamic strokes, when the contact topology exhibits significant temporal variation. Mechanistically, this correlation serves as a structural transfer function that remains robust across a wide range of operating conditions, because the load boundary profile is strictly dictated by the geometric conformity of the ball-socket pair rather than by fluctuating operating pressures. However, its envelope of validity is bounded by high-pressure operations that ensure continuous, positive contact between the ball and socket. Under severe transient dynamic reversals or low-pressure suction strokes, where inertial forces can induce micro separation or partial joint liftoff, this static equivalence must be augmented with dynamic adjustments to accurately resolve the evolving contact topology.

Table 2. Input for the parametric FEM study of the slipper

$2 * \alpha$ (°)	a (mm)	A_{eff} (mm^2)	$p_{contact}$ (MPa)
30	3.5	41.25	358.38
45	4.95	90.20	163.90
60	6.06	153.93	96.04
75	6.76	228.20	64.78
90	7	307.87	48.02

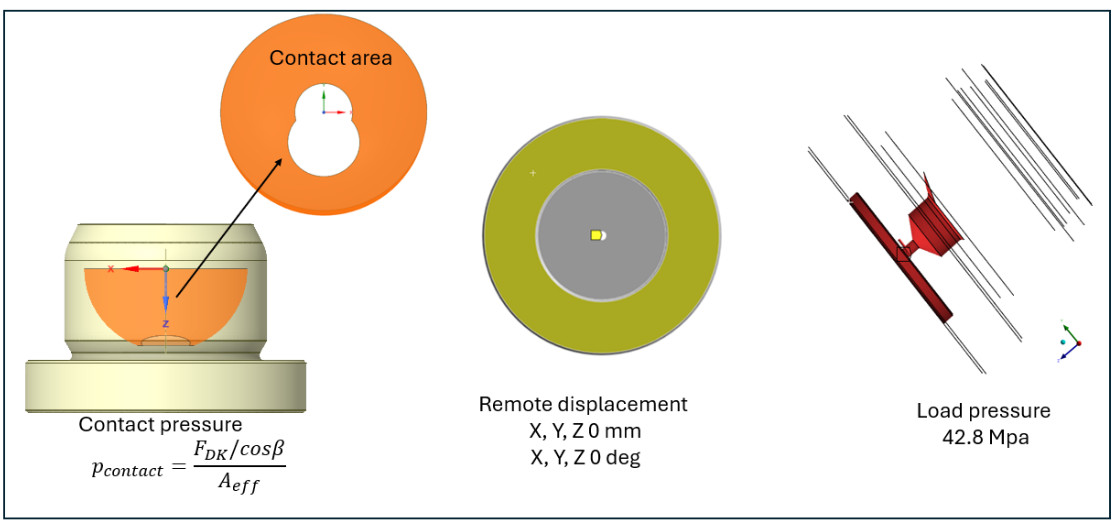

Figure 7. Contact Area Definition and Pressure Calculation Framework for the Ball–Socket Interface

A series of structural simulations was performed on the slipper to assess how variations in joint geometry influence the deformation of the sealing land. In this parametric study, the contact radius and the contact angle were selected as the primary independent variables. The objective was to determine which angular increments, reported in Table 2, produce deformation levels comparable to those obtained in the assembly level analysis for different radial clearances. Establishing this correspondence enables a direct comparison between the two parameters, ball-socket clearance and contact angle, in terms of their effect on the overall structural response of the slipper.

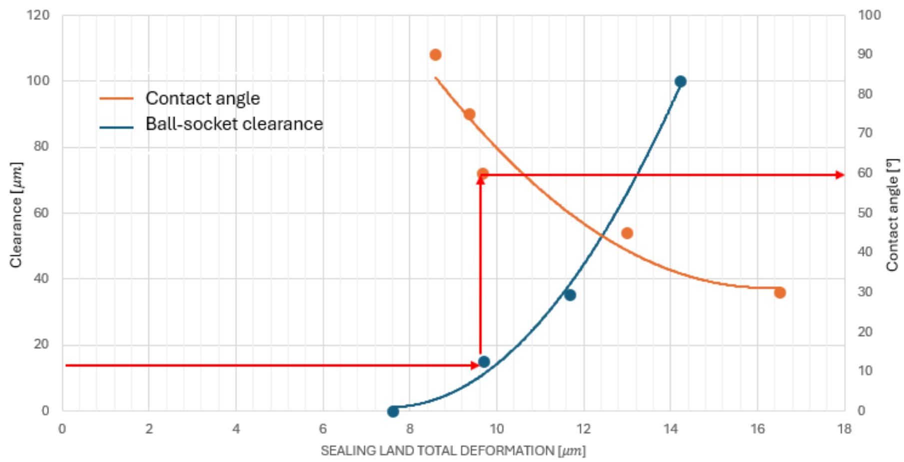

Figure 8. Mutual Influence of Clearance and Contact Angle on Slipper Sealing Land Deformation (simulation points and trend lines)

The comparison between the two parameters reveals that increasing clearance leads to a monotonic rise in sealing-land deformation, whereas increasing the contact angle has the opposite effect, progressively reducing deformation. By cross-referencing the two trends, an equivalence point emerges: a clearance of roughly 15 μm produces the same deformation as a 60° contact angle, both resulting in a total deformation of approximately 9.7 μm. This establishes a direct quantitative relationship between the two geometric parameters and provides a consistent basis for translating joint wear, i.e. clearance increase, into an equivalent change in contact angle. To further illustrate how the assumed contact geometry influences the structural response, Figure 9 compares the deformation field obtained using a full socket-contact assumption with that derived from the influence-matrix approach, where the contact radius corresponds to a 60° engagement angle.

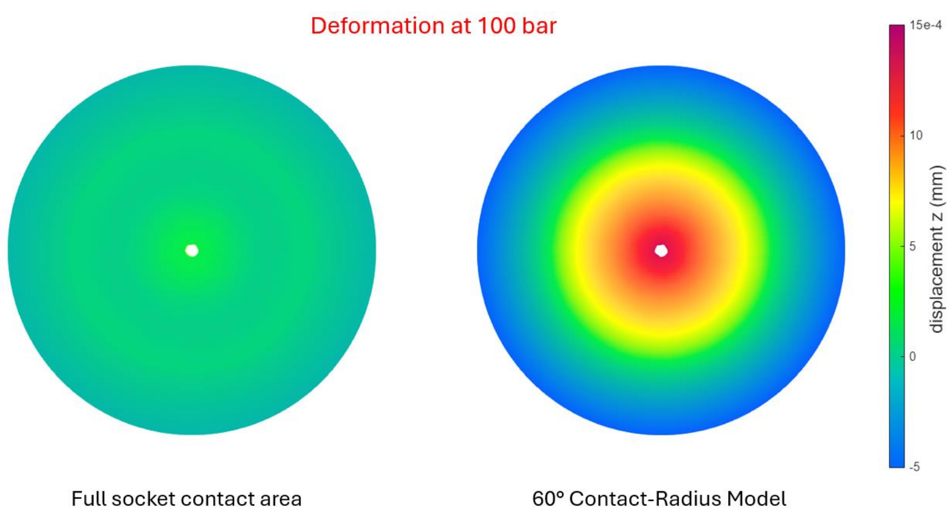

Figure 9. Deformation Response at 100 bar: Full Contact Patch vs. Contact Radius Derived from 60° Engagement

The comparison reveals a clear shift in the location and magnitude of the maximum deformation. Under the full contact assumption, the deformation remains nearly uniform across the sealing land, with only a slight central depression. In contrast, when the contact radius is restricted to the 60° region, the deformation becomes strongly localized: the maximum displacement occurs near the center of the slipper, directly under the reduced contact patch where the load is applied. This concentrated deformation produces a steeper radial gradient, with progressively smaller displacements toward the outer radius. The resulting profile is consistent with the tilting mode identified earlier, where central compression is accompanied by peripheral lift-off.

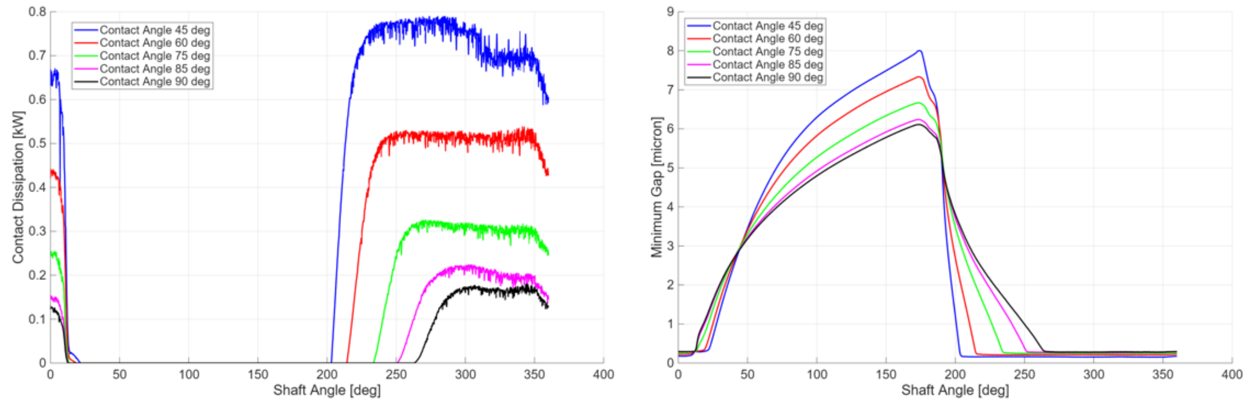

a b

Figure 10. a) Angular Evolution of Contact Dissipation b) Minimum Gap Height Over a Revolution for Different Contact Angles

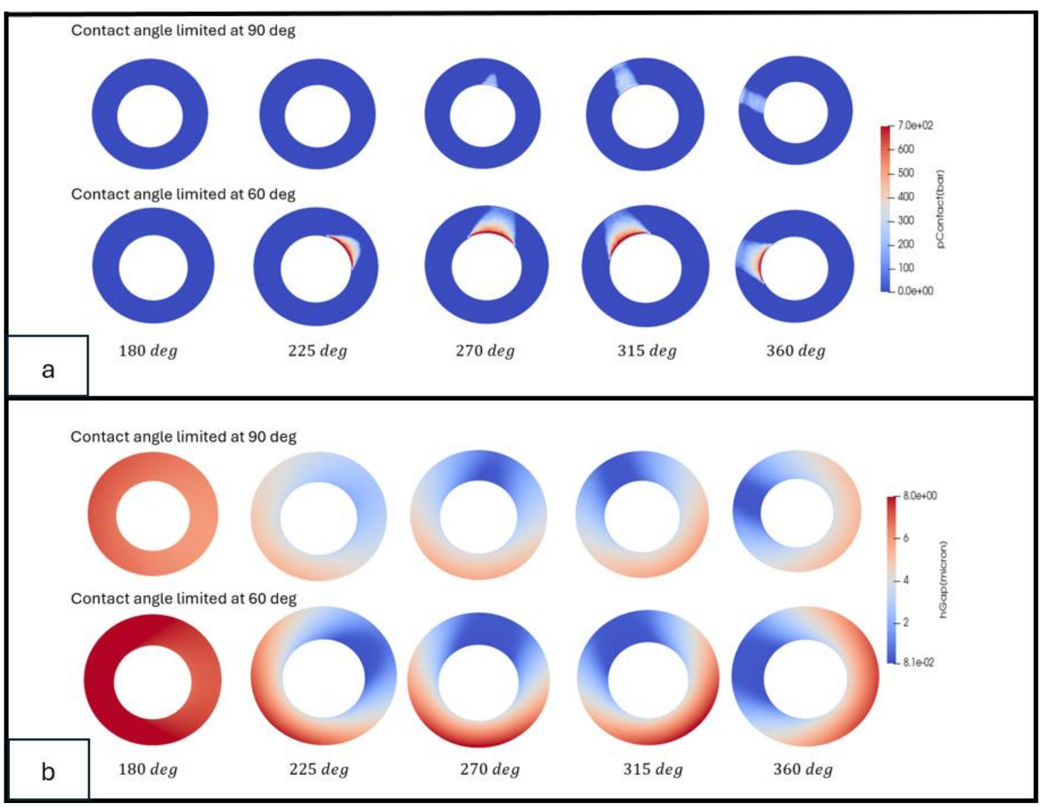

Figure 11. Angular Evolution of a) Contact Pressure, b) Film Thickness in the Slipper Pad Interface During the High-Pressure Stroke for a 90 degrees & 60 degrees Limited Contact Area

Figures 10 and 11 illustrate the strong coupling between film thickness, contact pressure development, and energy losses as the slipper rotates during the high-pressure stroke. Figure 10 shows that the minimum gap exhibits a clear dependence on the imposed contact area angle. When the contact area becomes more restricted, the minimum gap decreases more sharply and approaches near contact conditions over a wider angular interval. Correspondingly, the contact dissipation remains low when the film is still relatively thick but rises significantly once the gap collapses and stays elevated throughout the portion of the stroke where the interface operates in mixed or boundary lubrication.

Figure 11 further confirms this behavior by showing that the regions of minimum film thickness coincide with the angular positions where the mechanical load is concentrated. In these zones, the hydrodynamic pressure increases within the converging wedge and diminishes toward the diverging region, revealing a pronounced angular dependence of both pressure generation and film formation. The comparison between the 90° and 60° contact area constraints also highlights that a more limited contact area intensifies the pressure peaks and reduces the film thickness, thereby promoting higher dissipation and more severe lubrication conditions.

A smaller contact angle makes the slipper more unstable because the reduced load-carrying area cannot maintain a sufficiently thick hydrodynamic film. When the motor operates at high pressure, the slipper tends to tilt, locally squeezing out the oil film. This collapse of the lubricating wedge forces the interface into mixed or boundary lubrication, where the edges experience concentrated contact pressure. Consequently, frictional dissipation increases, and the risk of severe wear becomes significantly higher.

5. Conclusion

This work has demonstrated that the clearance between the piston ball and the slipper socket plays a decisive role in governing the mechanical and tribological behavior of the slipper swashplate interface. The coupled simulation framework developed here shows that even small variations in ball–socket clearance can significantly alter the slipper tilt, load distribution, and lubrication conditions throughout the high-pressure stroke. These geometric effects directly influence film formation, the balance between hydrodynamic and contact pressures, and the resulting energy-dissipation mechanisms. The results further reveal that the angular evolution of minimum film thickness, hydrodynamic pressure, and contact dissipation is strongly affected by the imposed 60° contact area constraint, underscoring the interface's sensitivity to both design and operating parameters. Overall, the findings confirm that ball–socket clearance is a critical design variable with direct implications for efficiency, wear, and long-term reliability in axial piston machines, and they provide a foundation for more accurate predictive models and improved motor optimization strategies.

Nomenclature

- F_{SP} Swashplate force [N]
- F_{HD} Hold on force [N]
- F_{aK} inertial piston force [N]
- F_{WK} Weight or normal reaction force [N]
- F_{TK} Friction force [N]
- F_{DC} Piston force [N]
- F_{SP} Swashplate reaction force [N]

- F_{spring} Spring Force [N]
- β Tilt angle between the slipper and swashplate [°]
- μ (dynamic viscosity) Dynamic viscosity of the lubricant (Pa·s)
- h (film thickness) Instantaneous fluid-film thickness between slipper and swash plate [m]
- dh/dt (time derivative of film thickness) Rate of change of film thickness [m/s]
- r_{outG} (outer radius of the gap region) Outer radius of the annular lubrication region [m]
- r_{inG} (inner radius of the gap region) Inner radius of the annular lubrication region [m]
- σ_{slipper} RMS roughness of the slipper surface [m]
- σ_{sp} RMS roughness of the swash-plate surface [m]
- Λ safety factor/separation parameter [adim]

References

1. Wu, J., Ma, L., An, G., & Han, H. (2023). *Squeeze film effect and its influence on the lubrication characteristics of slipper oil film under pressure pulse*.
2. *Li, D., Ma, X., Wang, S., Lu, Y., & Liu, Y. (2024). Failure analysis on the loose closure of the slipper ball-socket pair in a water hydraulic axial piston pump. Engineering Failure Analysis, 155, 107718. https://doi.org/10.1016/j.engfailanal.2023.107718*
3. Haidak, G., Wang, D., Shiju, E., & Liu, J. (2018). *Study of the influence of slipper parameters on the power efficiency of axial piston pumps*.
4. Meng, X., Ge, C., Liang, H., Lu, X., & Ma, X. (2020). *Lubrication characteristics of the slipper–swashplate interface in a swashplate-type axial piston pump*. Proceedings of the Institution of Mechanical Engineers, Part J: Journal of Engineering Tribology.
5. Sharif, K. J., Evans, H. P., & Snidle, R. W. (2012). *Modelling of elastohydrodynamic lubrication and fatigue of rough surfaces: The effect of lambda ratio*.
6. Shen, H., Zhou, Z., Guan, D., Liu, Z., Jing, L., & Zhang, C. (2020). *Dynamic contact analysis of the piston and slipper pair in axial piston pump*.
7. Schlegel, F., & Schmitz, K. (2025). *Geometric design of axial piston machine slipper-bearings made of high-performance plastics*.
8. Betti, A., Forte, P., & Ciulli, E. (2026). *An extension of Hertz's formula for the stiffness of conformal spherical contacts*.
9. Harris, R. M., et al. (1963). *The design and performance of hydrostatic slipper bearings*. Proceedings of the Institution of Mechanical Engineers.
10. Hooke, C. J., & Kakoullis, Y. P. (1978). *The effects of non-parallelism on the performance of slipper bearings*. In Proceedings of the 4th International Fluid Power Symposium.
11. Schenck, A., & Ivantysynova, M**.** (2016). *A transient thermo-elastic swashplate and slipper model*. International Journal of Fluid Power.
12. Tang, H., et al. (2019). *Impact of manufacturing tolerances on the lubrication performance of the slipper–swashplate interface*. Tribology International.
13. Chao, Q., et al. (2015). *Effects of ball-joint clearance on the slipper behavior*. Journal of Mechanical Science and Technology.
14. Canbulut, F., et al. (2014). *Effects of slipper geometry on the performance of an axial piston pump*.
15. Multics Documentation — Multics v4.1.0
16. https://engineering.purdue.edu/Maha/assets/docs/MulticsBrochure2022.pdf.
17. T. Ransegnola, L. Shang, and A. Vacca, "A study of piston and slipper spin in swashplate type axial piston machines," *Tribology International*, vol. 151, p. 106403, Nov. 2020.